Climate Dynamics (2022) 59:2363–2379
https://doi.org/10.1007/s00382-022-06214-3

Spatial patterns of extreme precipitation and their changes under ~ 2 °C global warming: a large-ensemble study of the western USA

David E. Rupp[1] · Linnia R. Hawkins[2] · Sihan Li[3] · Matthew Koszuta[4] · Nicholas Siler[4]

Received: 20 September 2021 / Accepted: 14 February 2022 / Published online: 4 March 2022

Abstract
Extreme precipitation events are expected to increase in magnitude in response to global warming, but the magnitude of the forced response may vary considerably across distances of ~ 100 km or less. To examine the spatial variability of extreme precipitation and its sensitivity to global warming with high statistical certainty, we use a large (16,980 years), initial-condition ensemble of dynamically downscaled global climate model simulations. Under approximately 2 °C of global warming above a recent baseline period, we find large variability in the change (0 to > 60%) of the magnitude of very rare events (from 10 to 1000-year return period values of annual maxima of daily precipitation) across the western United States. Western (and predominantly windward) slopes of coastal ranges, the Cascades, and the Sierra Nevada typically show smaller increases in extreme precipitation than eastern slopes and bordering valleys and plateaus, but this pattern is less evident in the continental interior. Using the generalized extreme value shape parameter to characterize the tail of the precipitation distribution (light to heavy tail), we find that heavy tails dominate across the study region, but light tails are common on the western slopes of mountain ranges. The majority of the region shows a tendency toward heavier tails under warming, though some regions, such as plateaus of eastern Oregon and Washington, and the crest of the Sierra Nevada, show a lightening of tails. Spatially, changes in long return-period precipitation amounts appear to partially result from changes in the shape of the tail of the distribution.

Keywords Extreme precipitation · Single model initial condition large ensemble (SMILE) · Generalized extreme value · Shape parameter · Orography · Climate change · Western North America

1 Introduction

Much of the storm water infrastructure in the US is built to withstand runoff generated by precipitation amounts that, in a stable climate, would occur only once every 10–100 years on average (Lopez-Cantu and Samaras 2018), while dams are designed to withstand much rarer events (Hossain et al. 2012). Quantifying the anthropogenic influence on extreme precipitation events at local-to-basin scales is therefore critical for understanding future flood hazard and its implications for water infrastructure.

Features of the landscape modulate the large-scale response of the hydrological cycle to anthropogenic greenhouse gas forcing (Diffenbaugh et al. 2005), resulting in spatially heterogeneous responses at meso- and finer scales in temperature (Rupp et al. 2017), winds (Letcher and Minder 2015, 2017), and precipitation intensity (Wallace and Minder 2021). The importance of topographic gradients to precipitation, and the societal relevance of extreme precipitation events, has long motivated the study of forced changes in precipitation extremes by using global climate model output downscaled with finer resolution regional climate models that more accurately represent a region's topography. Many

✉ David E. Rupp
david.rupp@oregonstate.edu

[1] Oregon Climate Change Research Institute, College of Earth, Ocean, and Atmospheric Sciences, Oregon State University, Corvallis, OR, USA

[2] Forest Ecosystems and Society, Department of Forestry, Oregon State University, Corvallis, OR, USA

[3] School of Geography and the Environment, University of Oxford, Oxford, UK

[4] College of Earth, Ocean, and Atmospheric Sciences, Oregon State University, Corvallis, OR, USA

studies have been done around the globe, but, for brevity, as examples we list here those whose geographical focus included western United States (US), and still only a subset of those: Diffenbaugh et al. (2005), Dominguez et al. (2012), Singh et al. (2013), Wehner (2013), Ashfaq et al. (2016), Huang and Ullrich (2017), Prein et al. (2017), Li et al. (2019a), Huang et al. (2020), Lopez-Cantu et al. (2020), Wrzesien and Pavelsky (2020), Mahoney et al. (2021).

Overall, studies show an apparent influence of mountains on the spatial pattern of changes in extreme precipitation over the western US (Singh et al. 2013; Prein et al. 2017; Huang et al. 2020; Mahoney et al. 2021). In some more recent studies (Huang et al. 2020; Mahoney et al. 2021), a general pattern emerges of larger percentage increases (though not necessarily larger absolute increases) in the leeward (eastward) side of major mountain ranges and smaller percentage increases on the windward (westward) side. This difference is often most conspicuous between the east and west sides of the Cascades in Washington and Oregon and the Sierra Nevada in California, north–south oriented mountain ranges that run roughly perpendicular to dominant winter wind directions.

However, attributing apparent changes in extreme precipitation to the imposed anthropogenic forcing in climate model experiments is hindered by the inherent internal variability of the climate system and by how well climate models simulate this internal variability (Deser et al. 2014; Poschlod and Ludwig 2021). Standard comparisons of, for example, two 30-year integrations (one reference state and one future state) from a downscaled global climate model poorly distinguish signal from noise. Examining the mean response from multi-model ensemble experiments (Dominguez et al. 2012; Wehner 2013; Ashfaq et al. 2016; Mahoney et al. 2021) partially addresses the problem by reducing the effect of internal variability and has the added benefit of likely canceling some model errors. However, averaging across models may smooth over the very feature of interest here, which is the finer-scale spatial heterogeneity of forced response in extreme precipitation. This smoothing may arise from different representations of the land surface where spatial resolutions, surface parameters (e.g., albedo or roughness), and land-surface process representations differ across models. Even where resolutions are similar, regional models may use different grid configurations. Moreover, the location of key features of the atmospheric circulation (e.g., jet stream) that affect where extreme precipitation events occur, as well as how these features respond to forcing, may vary across models.

Pseudo-global warming experiments offer an alternative method for improving signal to noise (Prein et al. 2017; Wrzesien and Pavelsky 2020). In such experiments, a future climate is generated by adding a mean climate perturbation to the regional boundary conditions of a reference (historical) integration. This perturbation is based on expected changes in the mean conditions predicted by global climate model runs. Constraining the boundary conditions of the future integration to that of the reference integration (albeit with a perturbation) greatly reduces the influence of interval variability. The downside of this approach is that it does not capture potential changes in storm dynamics, including shifts in the location or intensity of the midlatitude storm tracks, which could have a large impact on the spatial change of precipitation extremes.

An obvious way to improve signal-to-noise is to generate a single-model initial-condition (IC) large ensemble (SMILE), which is generated by running many simulations of the same experiment repeatedly but with a different initial state for each simulation. However, as the resolution of regional climate models becomes finer, the computational requirements become burdensome. For this reason, early studies on extremes using IC ensembles had relatively small ensemble sizes (e.g., five members in Singh et al. 2013), but experiments using ~ 50-member ensembles are rapidly becoming more common (Scinocca et al. 2016; Innocenti et al. 2019; Wood and Ludwig 2020; Huang et al. 2020; Singh et al. 2021).

Besides differences in experimental designs, a comparison of studies is complicated by the varied definition of "extreme". Most studies define "extreme" as the 95th or 99th percentile of daily precipitation, sometimes stratified by season (Diffenbaugh et al. 2005; Singh et al. 2013; Ashfaq et al. 2016; Wrzesien and Pavelsky 2020; Mahoney et al. 2021). However, measured against precipitation events that have sudden and large impacts on the environment and for the design of flood management infrastructure, such levels of precipitation would not typically be considered extreme. Uniquely, Huang and Ullrich (2017) chose a fixed threshold amount (40 mm day^{-1}) but the level of impact would vary greatly across space, so it is difficult to evaluate across a region as spatially heterogeneous as the western US. Fewer studies consider more extreme precipitation, such as the 20, 50-year (Dominguez et al. 2012; Wehner 2013; Li et al. 2019a), or even 100-year (Lopez-Cantu et al. 2020) return period of annual maximum of daily precipitation amounts. Yet, the "100-year" standard is widely used for more critical storm water infrastructure (Lopez-Cantu and Samaras 2018; Wright et al. 2019) while more rare events are of interest and concern beyond just storm water infrastructure considerations.

Studies of changes to rare extreme precipitation intensities such as Dominguez et al. (2012), Wehner (2013), and Lopez-Cantu et al. (2020), used fitted theoretical distributions, namely the generalized extreme value (GEV) or Pareto, to estimate return period values, sometimes extrapolating to return periods beyond the length of the model integration (Dominguez et al. 2012; Lopez-Cantu et al. 2020).

However, there is some danger in using such theoretical distributions to estimate values for return periods that are longer than, or even of roughly the same length as, the model integration itself: The parameter that controls the shape of the distribution and, therefore, the heaviness of the right tail, is poorly constrained in sample sizes typically available for many climate modeling experiments (Papalexiou and Koutsoyiannis 2013). Moreover, the theoretical distributions may provide a poor fit in some locations (Wehner 2013). Because of the large uncertainty due to small sample size, some studies do not allow the shape parameter to change under additional forcing (e.g., Brown et al. 2014; Fix et al. 2018), while others do (Dominguez et al. 2012; Wehner 2013; Lopez-Cantu et al. 2020; Ban et al. 2020).

To examine very extreme precipitation and its sensitivity to climate change, we use a uniquely large (16,980 years) IC ensemble of dynamically downscaled global climate model simulations. By driving a regional climate model with a large global model ensemble, we include the effects of changing large-scale atmospheric variability and not just the changing mean-state climatology. The size of the ensemble permits examining precipitation amounts, and their changes under approximately 2 °C of global warming above a recent baseline period, during very rare events (e.g., 100-year return interval and even higher of annual maxima) with higher statistical certainty than previously done. Moreover, because the regional model resolves key mountain ranges of the western US, we examine the spatial pattern of changes in relation to topography. We give special attention to the GEV shape parameter, because of its utility as an index of the heaviness of the distribution tail and of its relevance to water infrastructure design.

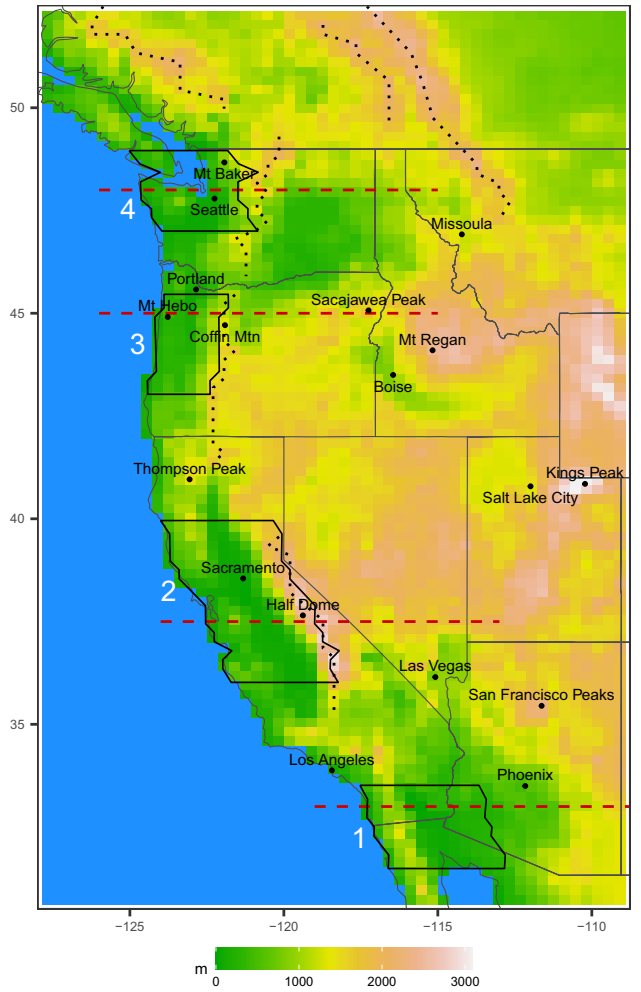

Fig. 1 Surface elevation in study area within the HadRM3P domain with features discussed in the text. Red dashed lines show the four transects, black-outlined polygons show the four regions identified by numbers "1" through "4", solid dots show selected locations of major cities and mountains, dotted lines show selected mountain range divides, and gray lines show political boundaries

2 Methods

Precipitation was simulated with the Hadley Centre Regional Climate Model (HadRM3P; Jones et al. 2003) at 0.22° × 0.22° horizontal resolution nested within the Hadley Centre Atmospheric Model (HadAM3P; Gordon et al. 2000) at 1.875° × 1.25° horizontal resolution with updated global and regional parameters (Hawkins et al. 2019; Li et al. 2019c). Both the regional and global model use the UK Met Office Surface Exchange Scheme 2 (MOSES2; Essery and Clark 2003) for the land surface. The grid cell size of the regional model (~25 km) is not only fine enough to resolve major mountain ranges but also the smaller coastal ranges (Fig. 1) which are some of the rainiest locations in the US.

It is important to note that the HadAM-RM3P pairing is not coupled to a dynamic ocean model, and sea surface temperature (SST) and sea ice are prescribed as boundary conditions. Excluding coupling can lead to reduced variance in the precipitation distribution and thus bias the change signal in an extreme value (e.g., Fischer et al. 2018). Still, uncoupled models are valuable tools, which do not suffer from problematic biases in sea surface temperatures and are less computationally demanding (He and Soden 2016a, b), the latter being a critical feature for the model simulations used in this study. Furthermore, Li et al. (2014) showed coupling had marginal effect on changes in seasonal mean precipitation over California while Dong et al. (2020) found little effect on changes in extreme winter or summer seasonal precipitation over North America.

We used two large ensembles of simulations. The first represents baseline climate conditions and the second represents a future wherein the mean global surface temperature is on average 2.26 °C warmer than the baseline. Both ensembles span 29 years (baseline: October 1987–December

2016; future: October 2047–December 2076). Transient concentrations of greenhouse gases, aerosols, and chemically active gases were based on observed values before 2006 and on Representative Concentration Pathway 8.5 (Meinshausen et al. 2011) from 2006 forward. Operational Sea Surface Temperature and Sea Ice Analysis (OSTIA; Donlon et al. 2012) provided the transient SSTs and sea ice fractions for the baseline period. For the future period, SSTs were generated using a "delta" (Δ) method: Smoothed transient changes in modeled SSTs (ΔSSTs) from the historical to the future period were added to the OSTIA SSTs. The ΔSSTs, and associated changes in sea ice fraction deltas, were derived from the global model CESM1-CAM5, following Hawkins et al. (2019). See, also, Ch. 3 in Hawkins (2019) for additional details on the modeling set-up, including spin-up and updates to the HadRM3P soil parameters.

Simulations were done on the volunteer computing platform weather@home (Massey et al. 2015; Guillod et al. 2017) configured for western North America (Mote et al. 2016). To facilitate parallel processing, simulations started in September of each year from 1986 to 2014 and from 2045 to 2074, with each simulation spanning a 28-month block. We used only the second complete water year (WY: October–September) from each simulation.

Simulations were performed with three sets of model parameters with altered values for parameters affecting moisture fluxes, cloud formation, and precipitation (See Table S1). These values were identified as among the best performing parameterizations in Li et al. (2019c), selected to minimize biases in regional seasonal mean temperature and precipitation while still attempting to account for parameter uncertainty by spanning a region of parameter space. Interested readers are referred to Li et al. (2019c) and Hawkins et al. (2019) for the detailed parameter improvement process. The three parameter sets were not chosen with a priori expectations of how they might lead to differences in daily precipitation extremes.

The IC ensembles were created by perturbing the global model's potential temperature field when initializing the simulation. For the baseline period, 100 IC ensemble members were generated per parameter set (300 members in total) per 28-month block. For the future period, 100 IC ensemble members per parameter set were completed per 28-month block except for three blocks ending in WYs 2050, 2060, and 2070 that had a different number of ensemble members per parameter set, and all fewer than 100. Therefore, to balance the number of ensemble members per parameter set, we used a subset of the future runs for the three blocks ending in WYs 2050, 2060, and 2070. For each year and each parameter set, we used only the number of ensemble members equal to the number of runs for the parameter set that had the fewest runs, resulting in 81, 76, and 73 ensemble members per parameter set for WYs 2050, 2060, and 2070, and 100 ensemble members for all other WYs. The total sample consisted of 2,830 WYs per parameter set (or 8,490 WYs in total) for the future period.

To have an equal the number of ensemble members in the baseline and future periods, we used only a subset of baseline runs consisting of 2830 WYs per parameter set. Specifically, the selection consisted of 81, 76, and 73 ensemble members per parameter set for WYs 1990, 2000, and 2010, and 100 ensemble members for all other WYs. Setting the number of ensemble members in WYs 1990, 2000, and 2010 to be the same as those in 2050, 2060, and 2070 is justified based on how future SSTs are generated: e.g., SSTs in WY 2050 are derived from observed SSTs in WY 1990 plus an estimated anthropogenic response.

Simulated 24-h precipitation accumulations were archived at a fixed daily time step (00 to 24 UTC). For each ensemble member, we extracted the WY maximum daily precipitation (R) and estimated the value of R at various return periods ranging from 2 to 1000 years (or, equivalently, at exceedance probabilities ranging from 0.5 to 0.001) for the baseline and future periods separately. Because our sample size was large ($n = 2830$), we first estimated the return period values empirically.

We compared HadRM3P return period values to those from the 1/24°-resolution gridded daily precipitation from the PRISM Climate Group. However, because the record length of the gridded PRISM data is relatively short (41 years) and because the spatial interpolation is guided by the climatological (30-year) averages of monthly precipitation (Daly et al. 2008), the PRISM data are not well suited for examining the shape of the far-right tail. Long-term station records, despite their much-reduced spatial coverage, are more appropriate for examining properties of the tails of precipitation distributions. Therefore, we also acquired daily precipitation station data from the US National Weather Service (NWS) Cooperative Observer Program (COOP; Wuertz et al. 2018) for all stations in the conterminous US west of −109 °E with records longer than 100 years (162 stations; see Table S2 for a list of the stations). For comparing right-tail heaviness of modeled with observed precipitation, we used a non-parametric, dimensionless statistic: the ratio of the 20-year return period WY maximum daily precipitation (RP20) to the 2-year return period WY maximum daily precipitation (RP2). This ratio was calculated directly from empirical quantile estimates. We chose RP20 for the numerator to achieve a robust statistic from the observations after a visual inspection of the return period curves for the station observations showed RP values above RP20 to be noticeably impacted by sampling noise (see supplementary Fig. S1).

Despite the large sample size of our simulations, it was still useful to characterize the frequency distribution of R using a theoretical distribution, in part to compare with other studies. The generalized extreme value (GEV) distribution is

commonly used for block maxima precipitation. The GEV cumulative distribution G for variable x is

$$G(x) = \exp\left\{-\left[1+\xi\left(\frac{x-\mu}{\sigma}\right)\right]^{-1/\xi}\right\}, 1+\xi\left(\frac{x-\mu}{\sigma}\right) > 0 \quad (1)$$

where μ, σ, and ξ are the location, scale, and shape parameters, respectively. Our interest is primarily in the shape parameter, which determines the heaviness of the right tail of the distribution (e.g., Papalexiou and Koutsoyiannis 2013). When $\xi = 0$, the right tail of the distribution is asymptotically exponential. Values of $\xi > 0$ produce heavy right tails (i.e., of power-law type without all moments finite), whereas $\xi < 0$ leads to bounded right tails (i.e., G reaches 1 at finite x).

To obtain dimensionless location and scale parameters that we could compare across all stations, we scaled precipitation by the mean of the WY maximum daily precipitation $\overline{R}$, i.e., $x = R/\overline{R}$ (Koutsoyiannis 2004). The shape parameter is unaffected by the scaling.

Because GEV parameters have been shown to be sensitive to estimation method (e.g., Koutsoyiannis 2004), we fitted the GEV distribution using both an L-moments and a maximum likelihood (ML) method. Both methods were applied using the R package *extRemes* (Gilleland and Katz 2016). We also tested a generalized ML and a Bayesian method (both available in *extRemes*) but both were much slower and more susceptible to non-convergence, which were important factors given the large sample size and large number of locations (11,700 grid cells).

Various measures exist of how well GEV distributions fit observations (e.g., Laio 2004) but we wanted a direct measure of bias in the fitted GEV distribution along the far-right tail of the climate model data, particularly spanning return periods of 100–1000 years. We quantified right-tail bias as

$$\text{Bias} = \exp\left[\frac{1}{n}\sum_{i=1}^{n}\log\left(\hat{x}_i/x_i\right)\right] \quad (2)$$

where x denotes all n simulated precipitation amounts that have empirically estimated return periods between 100 and 1000 years, $\hat{x}$ are the GEV-predicted precipitation amounts at each of the same empirically estimated return periods, and i indexes the return periods.

3 Results

3.1 Comparison of large ensemble with observations

The spatial pattern of extreme precipitation in the western US is strongly influenced by the topography, as illustrated by the 10-year return period WY maximum daily precipitation (RP10) in Fig. 2. Higher precipitation on the western and southwestern sides of mountains results from orographic enhancement and highest moisture transport coinciding with primarily westerly and southwesterly flow (e.g., Bracken et al. 2015). HadRM3P successfully reproduces the observed spatial pattern, albeit more coarsely due to the model's ~25-km spatial resolution. However, HadRM3P tends to generate too much extreme precipitation on the windward side of mountain ranges (Fig. 2). The bias is particularly high in the Sierra Nevada of California. This excessive orographic enhancement is also evident in the wet season (October through April) mean precipitation (Ch. 3 in Hawkins 2019; Li et al. 2015) so it is not simply a feature of extreme precipitation events.

None of the three model parameterizations produced a distinctly lower bias than the others, nor did they show distinctly different spatial patterns (not shown). For these reasons, we present each statistic (e.g., the RP20) as an average of the three parameterizations, unless otherwise noted.

The simulated RP20/RP2 ratio shows a non-random spatial pattern associated with major mountain ranges (Fig. 3). Lower values of RP20/RP2 are evident on the western side of, among others, the Sierra Nevada and Cascades Ranges, Rocky Mountains in both US and Canada, and Coast Mountains of British Columbia (BC), where values tend to be between 1.5 and 2. The highest values by far are on the leeward side of the Peninsular Ranges of Baja California, and eastward, where values are mostly between 3 and 5. Unfortunately, the locations and quantity of the stations do not permit a thorough comparison with the observed spatial pattern of RP20/RP2 (Fig. 3). However, simulated and observed RP20/RP2 values are positively and moderately correlated in space (Pearson correlation coefficient $r = 0.49$). Considering only grid cells containing station locations, median RP20/RP2 is 1.98 and 1.87 in the simulations and observations, respectively. 95% of simulated values fall within 1.55 and 2.91, compared to 1.55 and 2.47 in the observations.

3.2 Spatial patterns in right tail shape

The GEV shape parameter derived from the large ensemble is strongly associated with the windward and leeward aspects of major mountains, especially in those mountain ranges nearer the Pacific Ocean (see Fig. 4 with parameters estimated using L-moments). Negative values of ξ are most prominent along the windward side of the first two major orographic barriers to westerly/southwesterly flow, indicating that the tail of the distribution is bounded in these locations. East of these barriers, positive values (i.e., heavy tails) dominate, though negative values are still present along some western slopes of the Rocky Mountains. The largest positive values of ξ (those > 0.3) mostly occur on the leeward (eastward) side of the Peninsular Ranges of Baja California.

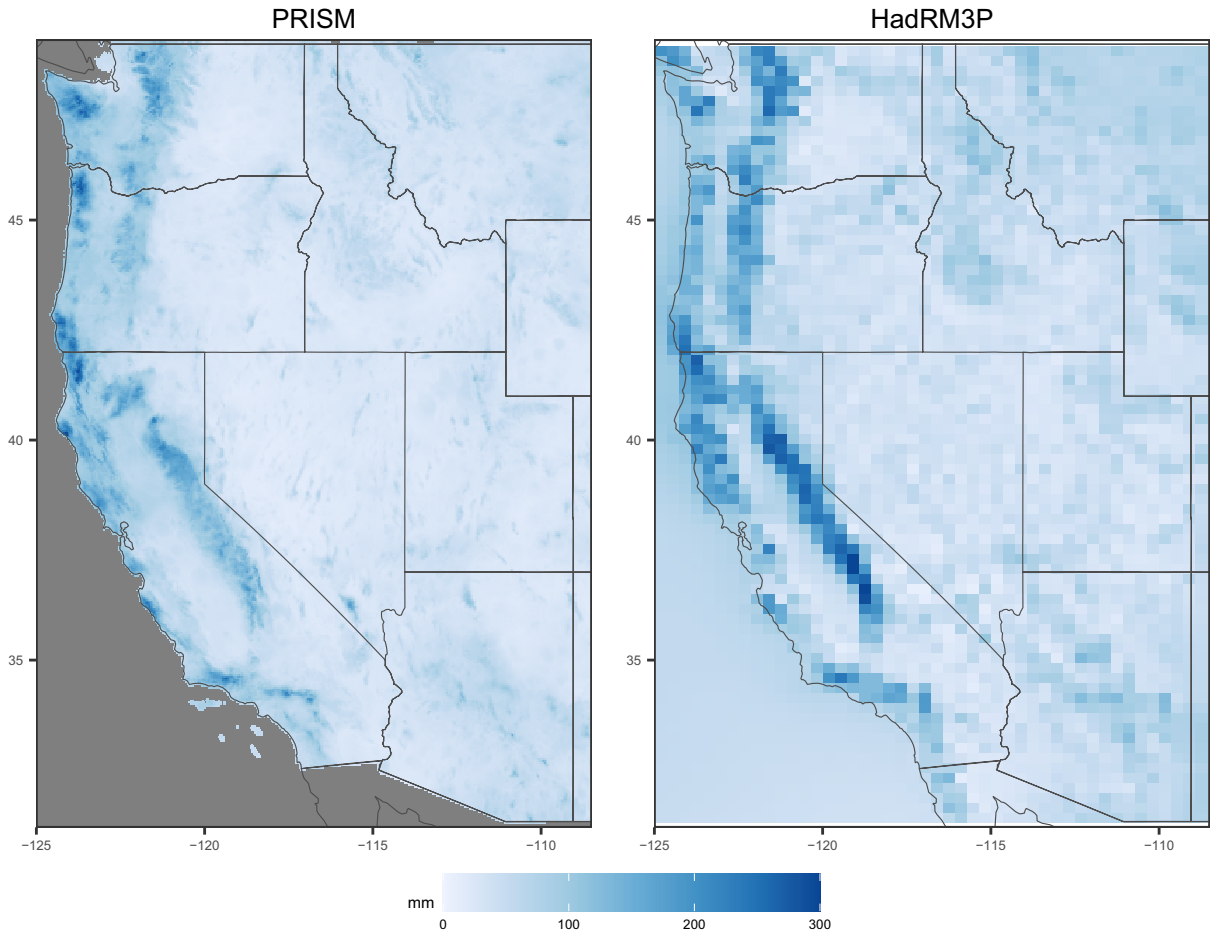

Fig. 2 Empirical 10-year return period for water year (WY) maximum daily precipitation (RP10) from (left panel) the 1/24°-resolution PRISM dataset for WYs 1982–2020 and (right panel) the 0.22°-resolution HadRM3P ensemble for the baseline period (WYs 1988–2016). For HadRM3P, the average of RP10 from the three parameter sets is shown

Compared to L-moments, ML estimates yet higher values of ξ in this region, (supplementary Fig. S2). Elsewhere, the spatial patterns of ξ produced from L-moments and ML are very similar.

In general, ML results in higher bias in the far-right tail compared to L-moments. In and around the Gulf of California region in particular, the ML-fitted GEV largely overpredicts the empirical values (see supplementary Fig. S3), so the high values of ξ over that region poorly characterize the actual heaviness of the right tail. Wehner (2013) and Ben Alaya et al. (2020a, b) also noted a poor fit of the GEV to simulations of the NARCCAP regional models and the Canadian Regional Climate Model (CanRCM4), respectively, around the region of Baja California.

ML also resulted in larger differences in bias between the baseline and future periods (see supplementary Fig. S4). Given that substantial differences in bias between periods would reduce confidence in estimates of the shape parameter's response to anthropogenic forcing, and that L-moments results in lower tail bias overall, we use L-moments estimates for the remainder of this analysis. Key figures showing results based on ML are provided in the Supplementary Information for comparison.

For the simulated precipitation, Fig. 5 provides example return period curves for six locations marked in Fig. 4 (see supplementary Fig. S5 for curves for the other 12 locations and Table S3 for a list of all 18 locations). Left column panels show windward aspect locations in (top to bottom) the Washington Cascades, Oregon Coast Range, and Sierra Nevada, all with $\xi < 0$. Right column panels show locations of major cities in the Willamette Valley of Oregon, Central Valley of California, and Salt River Valley in Arizona. These three valley locations, like most places in the study domain, have $\xi > 0$ and show no visual indication of asymptotically approaching a maximum precipitation value even by return intervals of a few thousand years.

How the variability across space in ξ seen in Fig. 4 manifests as variability in very extreme return period values may not be intuitive, so we compared ξ to a statistic whose hydrological relevance is more directly understandable: the

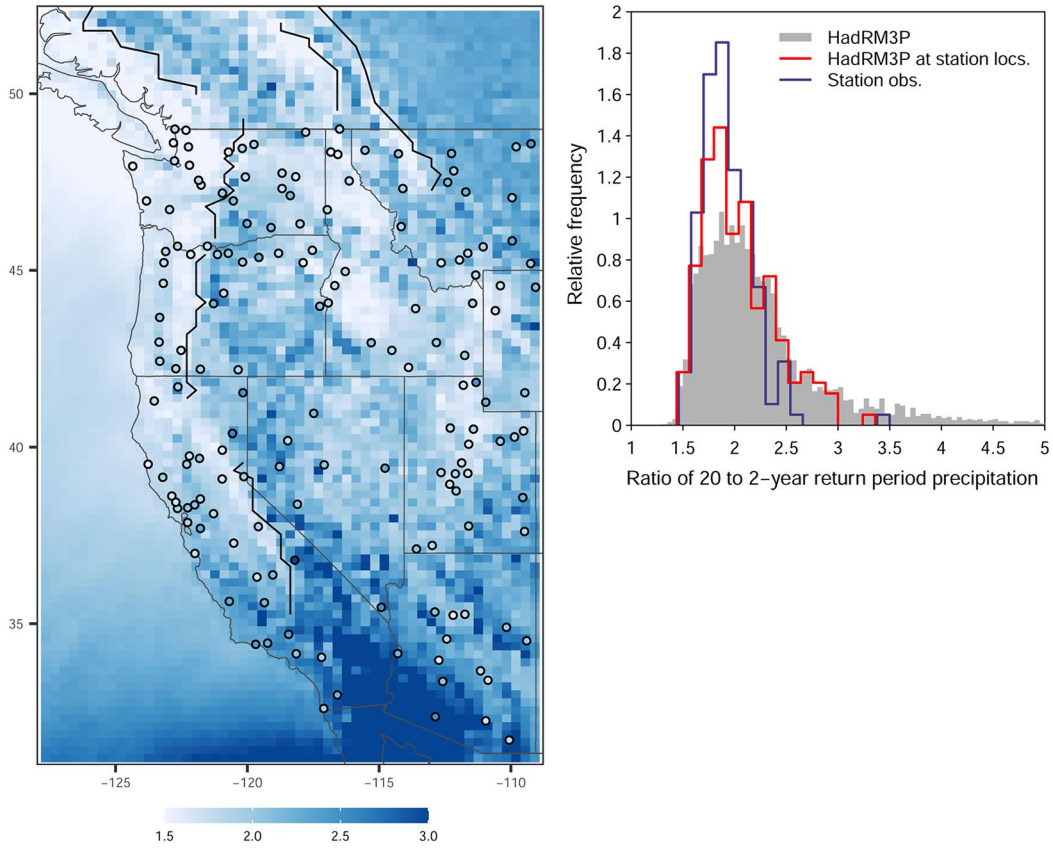

Fig. 3 (Left panel) Ratio of empirical 20-year (RP20) to 2-year (RP2) return period water year maximum daily precipitation from the HadRM3P ensemble during the baseline period. Colors are saturated above 3.0 to help distinguish the spatial heterogeneity across most of the domain. Circles mark station locations, color-shaded to their RP20/RP2 values. Black lines show selected mountain range divides (same as in Fig. 1). (Right panel) Frequency distribution of RP20/RP2 from observed precipitation at 162 stations, from the HadRM3P ensemble for the 162 grid cells containing the station coordinates, and from the HadRM3P ensemble for all land grid cells. Note the width of the histogram bins are different for the ensemble and the observations to more effectively visualize the distributions. Also, for the HadRM3P ensemble, the ratio is of the average of RP20 to the average of RP2 of the three parameter sets

ratio of the 1000-year return period water year maximum daily precipitation (RP1000) to the 10-year return period water year maximum daily precipitation (RP10), or RP1000/RP10. There is a strong spatial correlation between ξ and the empirical log(RP1000/RP10) ($r=0.95$ over land), indicating that RP1000/RP10 is useful as a proxy for right tail shape.

Although there is an exact, analytical solution of RP1000/RP10 as a function of the GEV parameters (e.g., Wehner et al. 2010), we found that the following linear equation is more easily interpretable and provides a satisfactory approximation over the range of ξ across the study area:

$$\log(\mathrm{RP1000}/\mathrm{RP10}) = b_1\xi + b_0 \quad (3)$$

with coefficients b_0 and b_1 estimated using standard least squares regression. Using all land cells in the regional model domain gives $b_1=2.84$ and $b_0=0.64$ with $R^2=0.90$. The value of b_0 implies that RP1000/RP10 is less than 1.90 (greater than 1.90) for negative (positive) values of ξ. Equation (3) also produces a 33% increase in RP1000/RP10 for every 0.1 increase in ξ. Stated another way, a difference in ξ from −0.15 and 0.15 corresponds to an increase in RP1000/RP10 by a factor of 2.3. If we take ξ = −0.15 and 0.15 as example values on the windward and leeward side, respectively, of a hypothetical mountain range, RP1000 is only 23% greater than RP10 on the windward side while RP1000 is 189% greater than RP10 on the leeward side.

3.3 Changes in extreme precipitation under global warming

Changes in extreme precipitation vary markedly across the western US and the spatial pattern of these changes shows the imprint of topography. Using RP20 as an example (Fig. 6), changes range from near zero to increases that exceed 40%. The largest percentage increases are in the southern Central Valley of California, Mojave Desert, and Imperial Valley south to the Gulf of California. Other areas

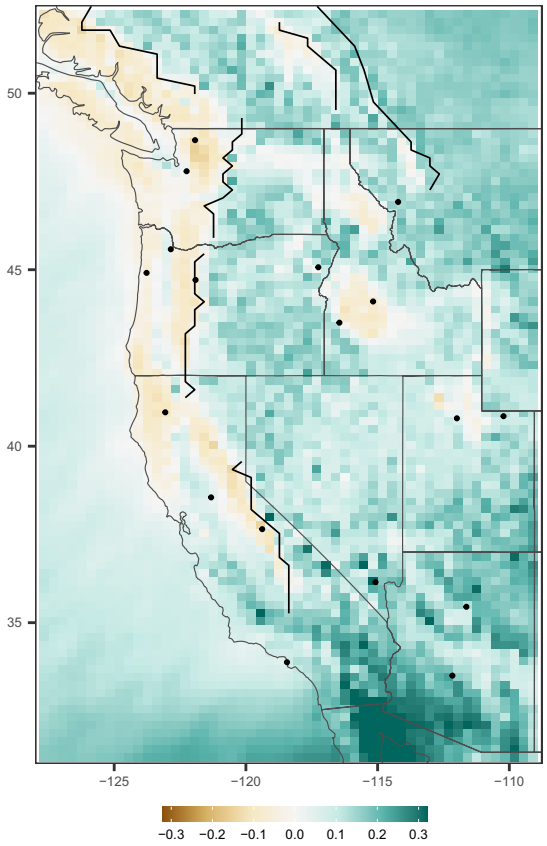

Fig. 4 GEV shape parameter ξ from the large ensemble for the baseline period with parameters estimated using L-moments. Green indicates a heavy right tail and brown indicates a bounded right tail. Black lines show selected mountain range divides and points indicate selected locations shown in other figures. Colors are saturated above $\xi > 0.32$ to help distinguish the spatial heterogeneity across most of the domain

along the coastal US with high increases relative to their surroundings include the Modoc Plateau in northeast California, Willamette Valley in western Oregon, Puget Sound in western Washington, and Columbia Plateau in eastern Washington. In contrast, smaller increases are detected on the much wetter windward slopes of adjacent mountains which form the first (the coastal ranges from Washington to California) and second (Cascades and Sierra Nevada) major topographic barriers to the dominant southwesterly flow directions during most major precipitation events. It is worth noting that changes in lowlands east of the coastal mountain ranges tend to be of similar magnitude as those over the ocean.

However, this pattern of smaller percentage increases in wetter climates is not present everywhere throughout the interior. For example, the dry Idaho Snake River Valley shows smaller increases in RP20 than do the wetter Rocky Mountains immediately to the north and northwest.

The spatial patterns described above largely persist for other extreme return periods (see RP10 and RP100 in Fig. 7), although the percentage changes tend to increase with longer return periods (see supplementary Fig. S6), consistent with other results (Li et al. 2019b). The spatial similarity across return periods indicates that these patterns are robust and not just the result of selecting a particular return period. The patterns become less well-defined as return periods become longer (Fig. 7, going left to right), though we do not know how much this reflects a real difference in the response of the most extreme precipitation events versus simply a lower signal-to-noise ratio. It is notable, however, that the patterns in California and western Oregon and Washington are the most persistent across a wide range of return intervals (at least from RP10 to RP1000).

The association of percentage changes in extreme precipitation with orography within the first several hundreds of kilometers from the coast is clearly evident in a set of four latitudinal transects ranging from northern Washington to southern California (Fig. 8, right column). Moving from west to east, the magnitude of increase in RP20 declines near the coastline and along the windward slope of the first topographic barrier. Past the first topographic divide, the magnitude of increase rises until reaching a maximum near the valley bottom, then declines once again along the windward slope of the second topographic barrier. Between the coast and the crest of the second topographic barrier, percentage changes in RP20 have a strong inverse relationship with the baseline RP20 (Fig. 9). Percentage changes in the dryer valley bottoms are frequently more than double those in the wetter mountain ranges. Further east, the relationship of precipitation change with topography becomes less clearly defined (Fig. 8, right column). The patterns described above are similar for RP10, RP100, and RP1000, although percentage increase in precipitation tend to be larger at longer return periods (supplementary Fig. S7).

Like our results, Li et al. (2019a; see their Fig. S3) and Li et al. (2019b; see their Fig. S7) also show larger increases in southern California than elsewhere in the western US. However, their results show less fine-scale variability than we present, which is likely due in part to the coarser resolution of their model (CanRCM4 at 50-km resolution) and the spatial pooling of neighboring grid cells they do to reduce the uncertainty from internal variability. Within California, our results are also consistent with Huang et al. (2020), who examined changes in precipitation from extreme atmospheric rivers in California based on the 40-member ensemble of ten-year long integrations from the Community Earth System Model Large Ensemble Experiment (CESM-LENS) and multiple nesting of a Weather Research and Forecasting Model (WRF) down to 3-km resolution, with anthropogenic forcings comparable to ours (RCP8.5; 1996–2005 vs.

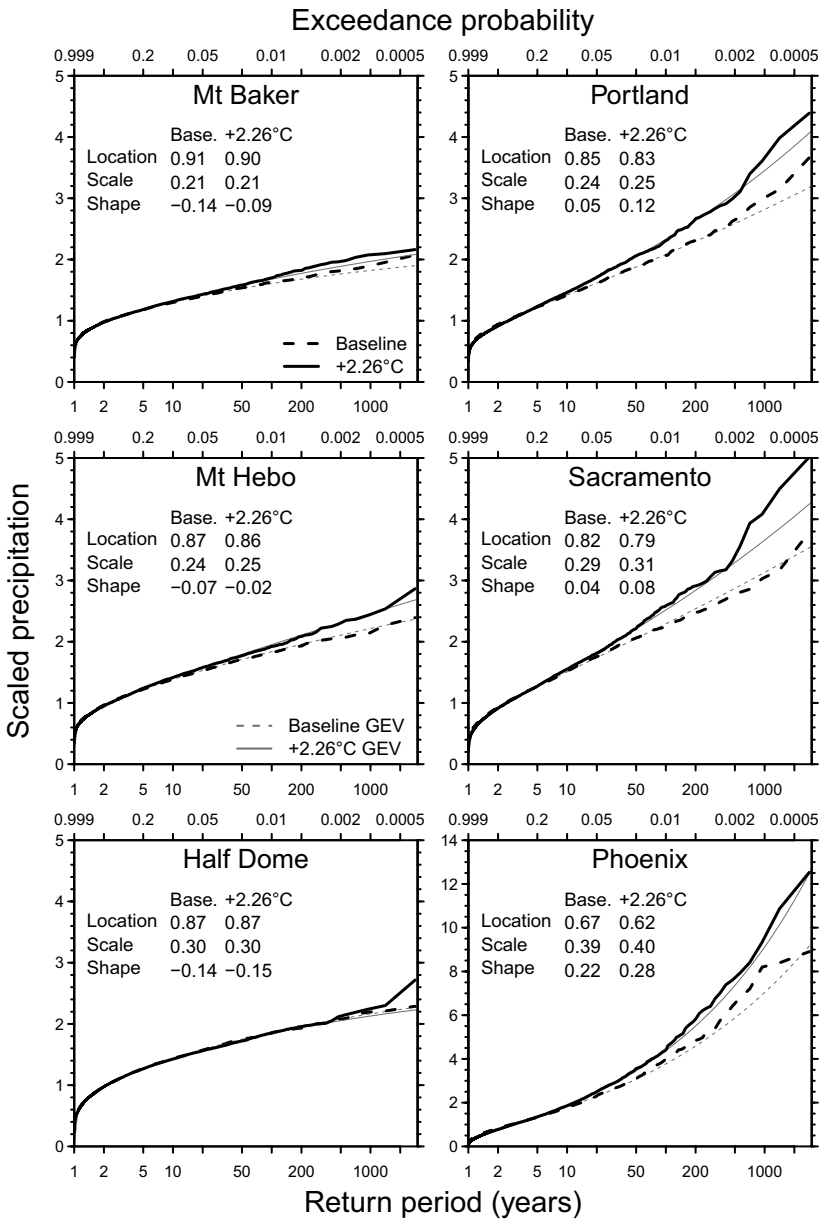

Fig. 5 Return period (exceedance) values of water year maximum daily scaled precipitation for the baseline (Base.) and future (+2.26 °C) period for grid cells at selected locations in mountains (left column) and valleys (right column). Heavy black lines show the empirical distributions and thinner gray lines show the fitted GEV distribution using L-moments. Note that Phoenix has a different vertical scale than the other locations

2071–2080). They report increases of 25–50% in the Central Valley compared to 10–30% along the western slopes of the Sierra Nevada, which are similar to the ranges in Fig. 8 (Region 4). As in Huang et al. (2020), we also found larger percentage increases in the southern Central Valley than in the northern Central Valley (Figs. 6 and 7).

These differential changes across space are statistically significant and the statistical power of a ~ 100-member ensemble is evident in Fig. 8. (Note: Unlike other figures that show averages of the changes from the three parameterizations, Fig. 8 shows results from only one parameter set to isolate the effect of IC ensemble size. Differences between parameter sets generally fall within the sampling noise so are not discussed here.) Based on width of the bootstrapped 95% confidence intervals (e.g., Rupp et al. 2017), we can detect changes from baseline in excess of about ± 5% using the large ensemble, though the width of confidence intervals varies somewhat in space. More importantly for this study of spatial patterns, we can similarly detect significant differences in response across space of at least ± 5%. In contrast, ten ensemble members would only detect changes greater than about ± 15 to 20%, whereas detection is effectively hopeless with a single ensemble member. It is important to note that the number of ensemble members required to achieve a certain confidence interval pertains to our setup without dynamic ocean coupling and we expect intervals would be wider in coupled model experiments and narrower in pseudo-global warming experiments.

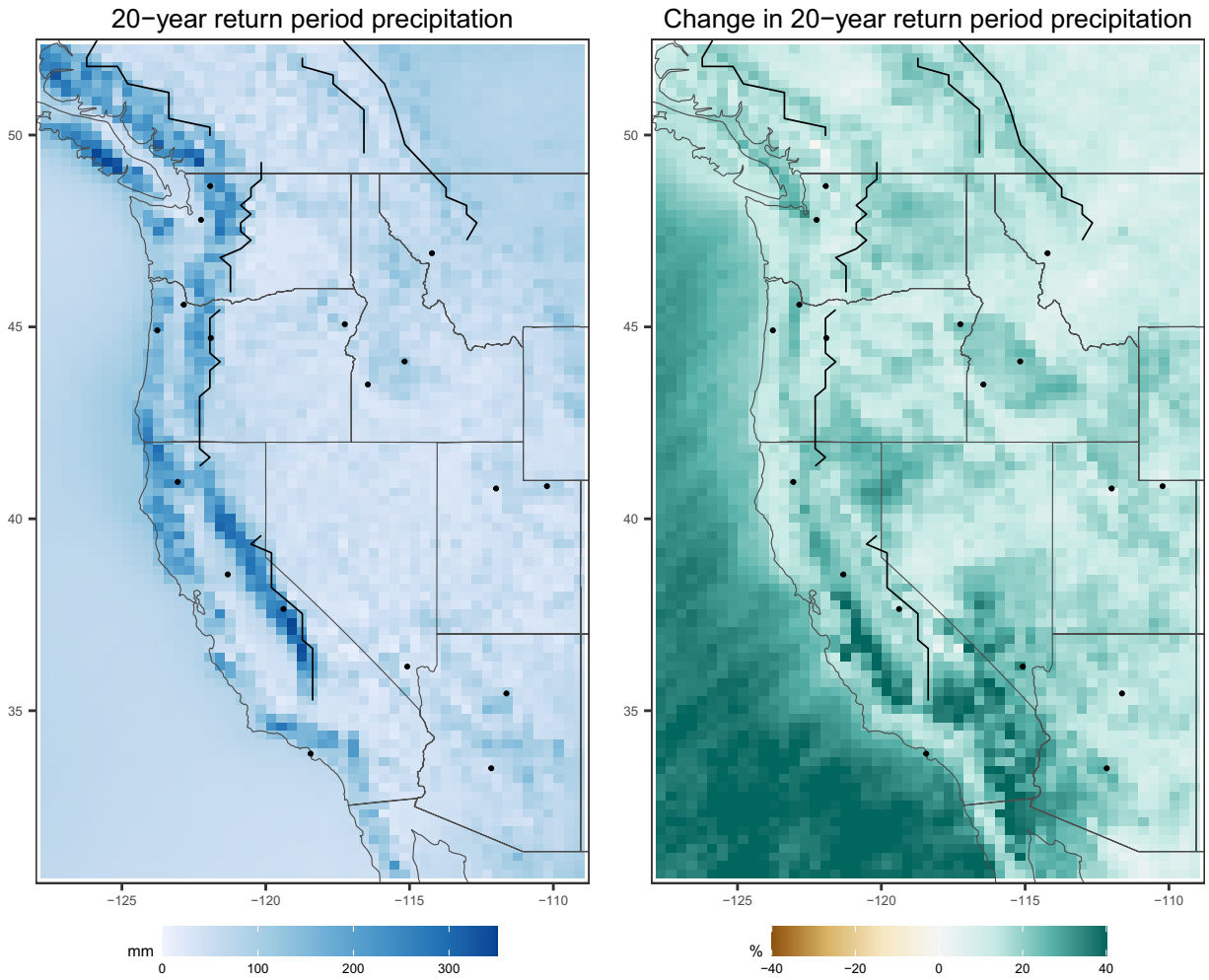

Fig. 6 (Left panel) Empirical 20-year return period water year maximum daily precipitation (RP20) for the baseline period. (Right panel) Percentage change in RP20 between the baseline and future (+2.26 °C) period. In both panels the average from the three parameter sets is shown

Changes in the shape of the extreme value distribution also show distinct non-random spatial patterns (Fig. 10; see supplementary Fig. S8 for results based on ML), with changes in ξ ranging from −0.09 to +0.12 across the model domain. Decreases in ξ, indicative of tails becoming lighter, occur east of the Coast Mountains of BC, the Cascades, and along the spine of the Sierra Nevada. In the case of the Cascades, decreases extend for several hundred kilometers east of the topographic divide. Other areas with decreases are not so clearly associated with the leeward side of a major north–south mountain range. These include the decreases west of the divide of the North Cascades where they extend into Canada, the Snake River Plain in Idaho, and the western part of the Rocky Mountains in central Idaho. Increases in ξ, indicative of tails becoming heavier, cover more of the domain than do decreases. The largest increases occur west of the Coast Mountains of BC, west of the Cascades, and in the Central Valley of California east of the Peninsular Ranges of Baja California.

We assume that the larger changes in the shape parameter are primarily a response to the increased anthropogenic forcing between the baseline and future periods, but the change in the shape parameter could also be affected by different degrees of low-frequency non-stationarity within the two periods. The future period is subjected to a higher rate of increase in anthropogenic forcing within its 29-year period than is the baseline period, so it is conceivable that this difference alone could broaden the distribution in the future period, resulting in a larger ξ (i.e., more positive or less negative). As a test, we first calculated the land pixel linear trends in water year maximum daily precipitation within the baseline and future periods (supplementary Fig. S9). We reasoned that a higher absolute value of a linear trend with a period (i.e., greater non-stationarity) would lead to a broader distribution and possibly larger ξ and, therefore, the absolute value of the future trend minus the absolute value of the baseline trend (Fig. S9) would be positively correlated with the change in ξ if within-period non-stationarity were an

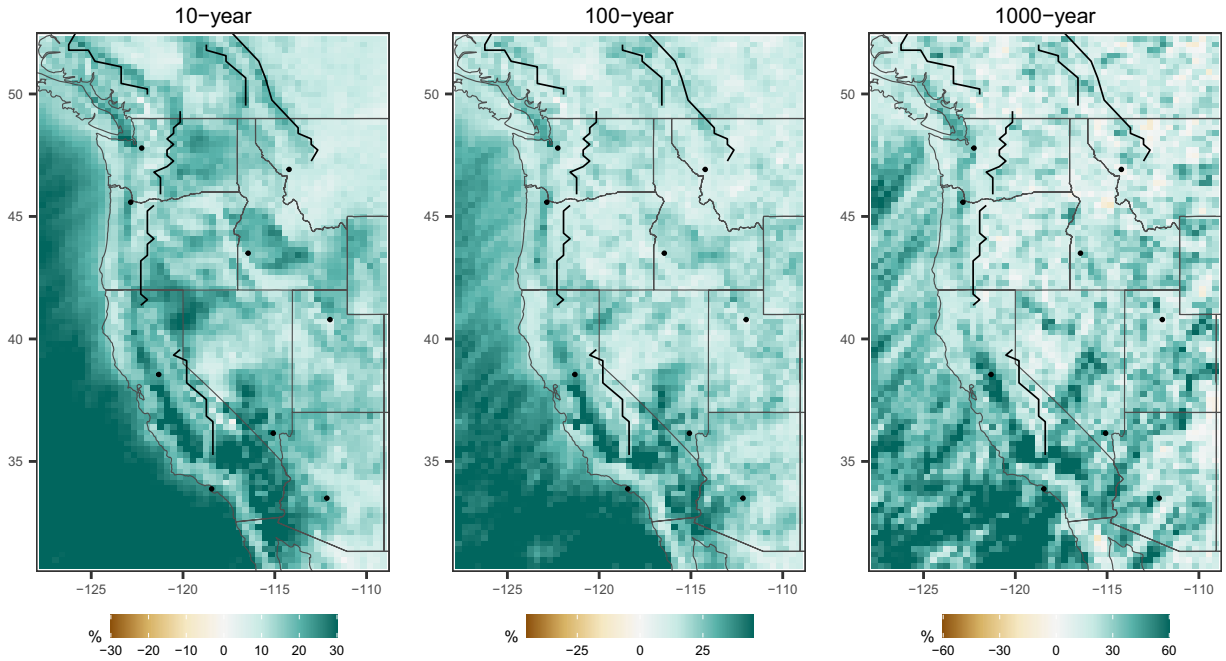

Fig. 7 Change (%) in the empirical 10 (left), 100 (center) and 1000-year (right panel) return period water year maximum daily precipitation (RP10, RP100, and RP1000). Black lines show selected mountain range divides and points indicate selected locations shown in other figures. The average of the return period values from the three parameterizations is shown. Note the color scales are different for each panel

important factor. We found no spatial correlation ($r = 0.03$) between this difference of absolute values of the trends and the change in ξ, implying that differences in non-stationarity between the periods have a negligible influence on the spatial pattern of between-period changes in ξ.

4 Discussion

4.1 Heaviness of the tail

The first main result of our analysis is the windward/leeward spatial structure of the shape of the distribution tail arising in the large ensemble, particularly apparent along the west coast of the US and Canada. In the interior of the US, the windward/leeward pattern is less apparent and heavy tails dominate. In the interior, extreme precipitation events are less centered on the winter months when stratiform systems dominate and are more distributed across warmer months (supplementary Fig. S10) where convection plays a larger role and the direction of moisture transport during extreme events is not as singularly oriented (i.e., westerly and southwesterly) throughout the year (Kunkel et al. 1999; Bracken et al. 2015).

There are few similar studies against which to compare our findings for the western US. Ben Alaya et al. (2020a, b) used a smaller (35-member) ensemble from a regional climate model to estimate the GEV shape parameter ξ across North America. The coarser resolution of their climate model (0.44°) and the greater spatial extent of their analysis domain reveal less spatial detail (see their Fig. 1) but a relationship between ξ and topography is still visible. For example, similar to our results, negative values of ξ are prominent west of the Sierra Nevada, Cascade, and Coast Mountains (BC) while the largest values of ξ occur on Baja California and surroundings. Fix et al. (2018), using a 30-member ensemble of 1°-resolution global climate runs, also show negative values of ξ in California (except for southernmost end), western Oregon, and most of Washington and Idaho, with mainly positive values elsewhere in the western US. However, neither Fix et al. (2018) nor Ben Alaya et al. (2020a, b) discuss the spatial pattern of ξ, or its causes, across the western US.

Using daily observations from a large number of stations around the globe, Ragulina and Reitan (2017) found a statistical relationship between ξ and elevation. However, they only used 17 stations in the western US (median ξ of 0.07), where they did not find statistical evidence against simply assuming a regionally constant value of ξ. Their findings generally support prior studies arguing for applying a positive value of ξ globally (Papalexiou and Koutsoyiannis 2013) if not even a universal value (of roughly 0.1) (Koutsoyiannis 2004; Wilson and Toumi 2005), given the difficulty in constraining ξ for any single station.

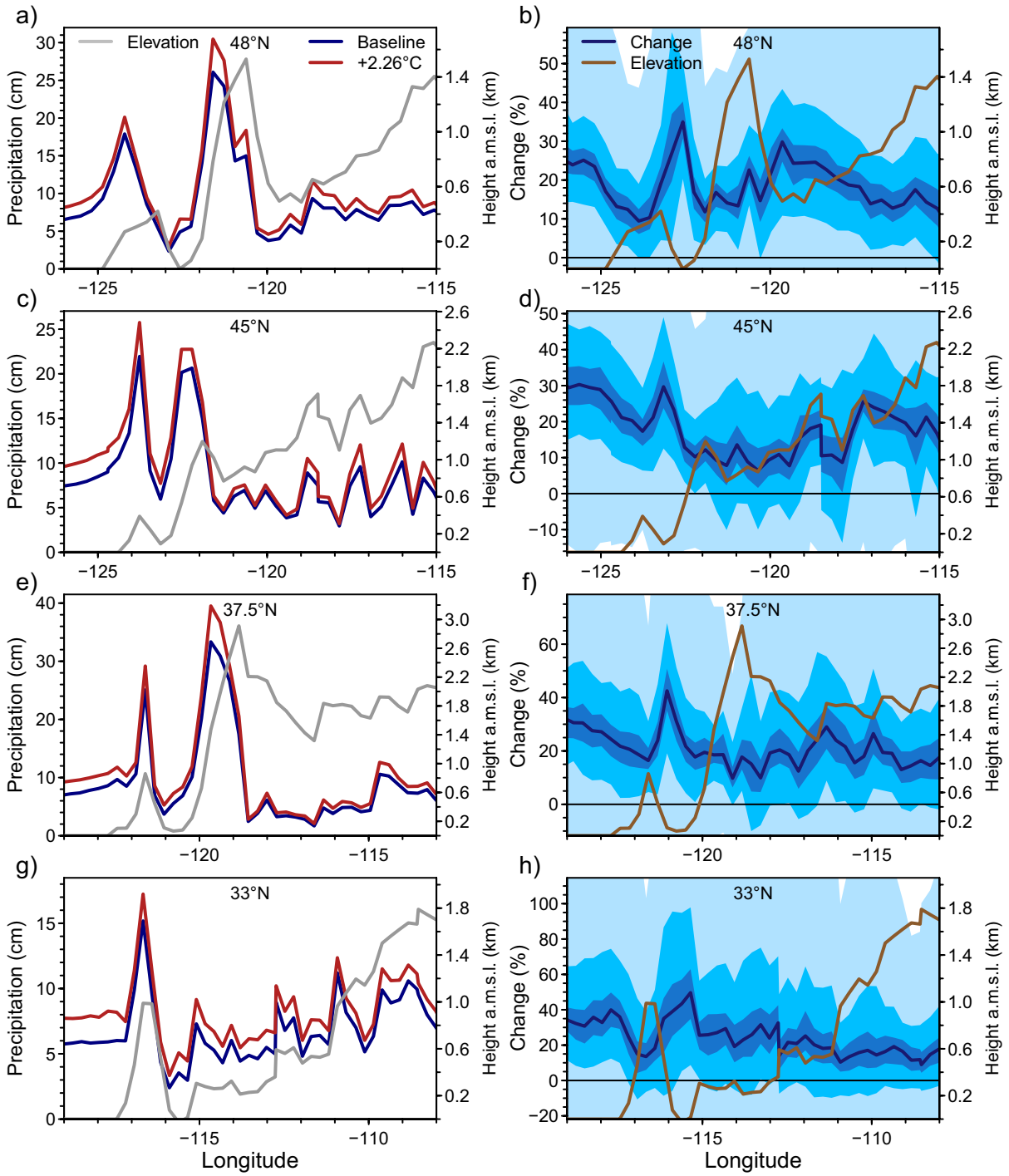

Fig. 8 (Left column) Empirical 20-year return period water year maximum daily precipitation (RP20) for the baseline and future (+2.26 °C) period from simulations using parameter set #1 along the four longitudinal transects shown in Fig. 1. (Right column) Percentage change from the baseline to the future period along the same four transects (dark line). Dark, medium, and light blue shading show the 95% confidence intervals using 1, 10, and ~100 ensemble members per year, respectively. Also shown is elevation along each transect. Note that the precipitation and elevation y-axis ranges differ for each transect

In contrast, Dyrrdal et al. (2016), using observation-based gridded data, found a tendency for negative values of ξ to occur in wetter regions of Norway, typically the windward (west) side of the Norwegian mountain range. They suggested the influence of orographic enhancement as a mechanistic argument for the spatially varying ξ across Norway.

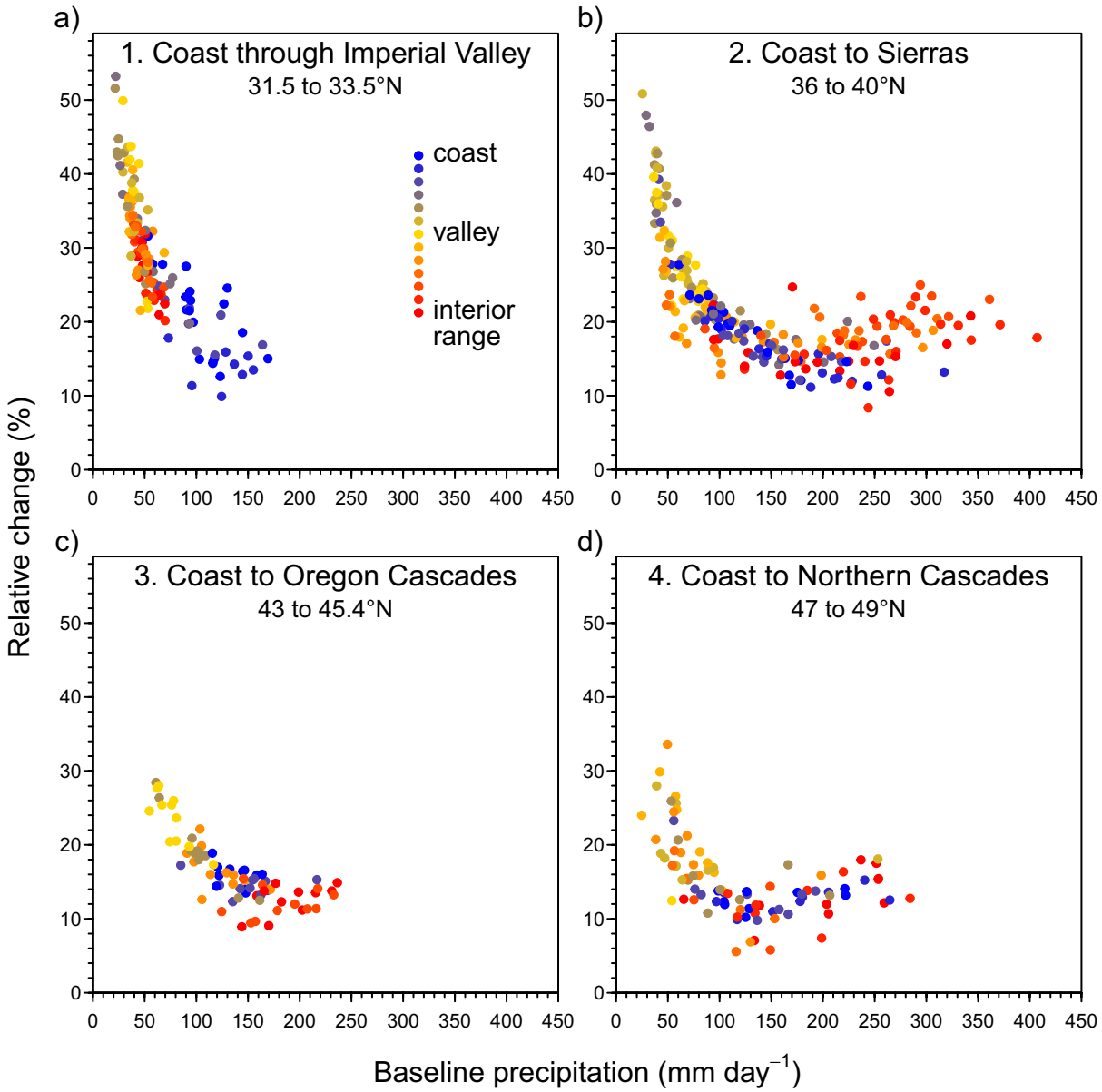

Fig. 9 Change (%) in the 20-year return period water year maximum daily precipitation (RP20) vs. the baseline RP20 from the large-ensemble simulations. Each symbol represents a grid cell in one of the four regions outlined in Fig. 1: **a** Coast through the Imperial Valley, **b** coast to the Sierra Nevada, **c** coast to Oregon Cascades, and **d** coast to Northern Cascades. Symbols are color-coded by their relative distance eastward from the coast in each region, such that blues generally represent the coastal mountains, yellows the valleys to the east of the coastal mountains, and reds the mountain range or hills to the east of the valleys. Values shown are the average of the return levels from the three parameter sets

Given that extremes in orographic enhancement are influenced by the wind speed orthogonal to the mountain range, it follows that the shape of the distribution of extremes wind speeds will be a control on ξ. The relative roles of extremes in wind speed and water vapor in determining the shape of the precipitation tail merit further study.

In a global study of over 22,000 station records, Cavanaugh et al. (2015) concluded that mixing of different precipitation types—i.e., those generated by different types of weather systems—produces heavier power-law tails. They highlight California as an example, attributing the lighter (more exponential) tails there to the dominance of one precipitation type (frontal systems). They also ascribe heavy tails in winter to the Cascades, which they attribute to a mixing of systems. This latter conclusion is questionable, however, given the dearth of long-term stations in the mountains and very low signal-to-noise obscuring differences across distances less than 1000 km. We also find generally heavier

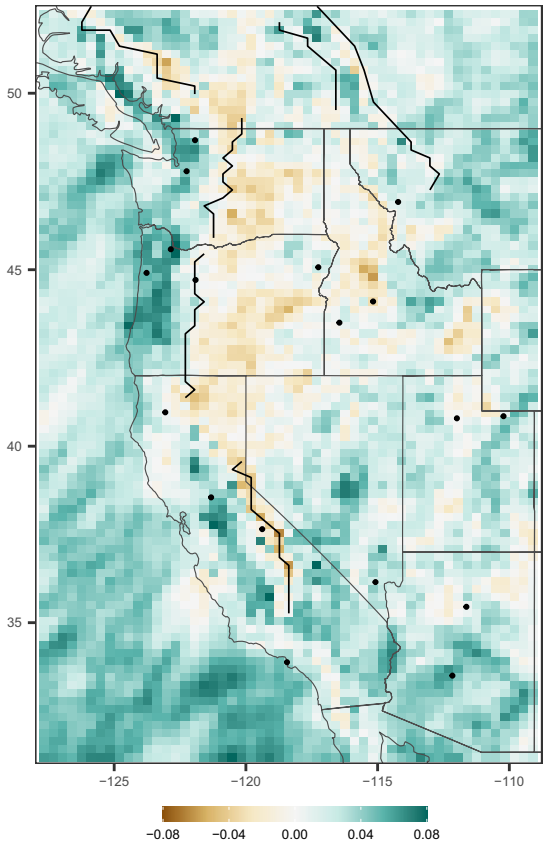

Fig. 10 Change in GEV shape parameter (future—baseline) with parameters estimated using L-moments. Green indicates a change towards a heavier right tail and brown indicates a change toward a lighter or bounded right tail. Black lines indicate selected mountain range divides and points indicated selected locations shown in other figures. Colors are saturated above 0.08 to help distinguish the spatial heterogeneity across most of the domain

tails in the interior west where precipitation types are more mixed, so repeating our analysis by season to help isolate the dominate precipitation type may yield insight.

4.2 Spatial variability in changes of extreme precipitation

Our second main result is the spatial structure of the percentage change in extreme precipitation under global warming. This spatial structure is important because it affects where runoff generation may be more impacted. As an example, discharge in large West Coast rivers, such as the Willamette River in western Oregon, derive most of their flood waters from the windward side of the major north–south oriented mountain ranges. Projected percentage changes in extreme precipitation are lower on these windward slopes than in surrounding areas, suggesting the effects of changing intensity will have a smaller effect on such rivers. In smaller lowland basins, including those with drainage from the leeward sides of coastal mountains, and in most urban areas, percentage increases in precipitation are much larger, implying a larger increase in risk of localized flooding in such areas. These impacts, however, do not consider the effects of changing precipitation phase from snow to rain, which are expected to contribute greatly to increases in extreme river discharge in the region (Chegwidden et al. 2020).

The pattern of differential windward-leeward changes from the west coast through the first and second major roughly north-to-south oriented topographic barriers is consistent with results from idealized experiments (Siler and Roe 2014; Shi and Durran 2015, 2016) and experiments using the actual topography at fine (3-km) resolution (Huang et al. 2020). Several mechanisms may contribute to this result. For example, Siler and Roe (2014) argue that, due to simple thermodynamics, the pattern of windward condensation will shift upward with warming. This may in turn contribute to a downstream shift in the spatial pattern of surface precipitation, resulting in larger fractional increases in the lee of a mountain range. In addition, other studies have identified changes in mountain-wave dynamics as a potential reason for weak changes in precipitation on windward slopes (Shi and Durran 2015). More complex patterns of change in the interior may reflect a more diverse range of moisture sources and flow directions. Further research is needed to fully understand the spatial pattern of extreme precipitation change and its governing mechanisms.

Changes in the GEV shape parameter also show non-random structure, with large variations in changes in ξ across relatively short distances (e.g., from west to east across the Cascades divide). With projected changes in ξ ranging mainly from about -0.05 to $+0.1$, the impacts are consequential. As noted above, a 0.1 increase in ξ implies about a 33% increase in RP1000:10. Also, the spatial pattern of changes in ξ (Fig. 10) bears resemblance to the percentage change in RP100 (Fig. 7), suggesting that the changes in ξ contribute in part to the spatial pattern of changes in extreme precipitation. Spatially, changes in ξ are positively correlated ($r = 0.38$) with percentage changes in RP100.

The simulated changes in ξ under global warming contradict Wilson and Toumi (2005) who, based on theoretical reasoning and an analysis of long-term records around the globe, argued that the shape of tail should be largely unaffected by climate change. Our findings, along with others showing a projected increase in heavy-tailed distributions over northeastern North America (Innocenti et al. 2019), indicate that the dynamic mechanisms driving projected changes in tail shape merit further investigation.

One limitation of this study is that it relies on just a single climate model (albeit with three different sets of parameterizations). This model generally does well at representing the spatial pattern of precipitation across the western US, but it is not without biases. In particular, it tends to overestimate

the degree to which precipitation is enhanced by orography, especially in the Cascades and Sierra Nevada. We do not know whether or how this bias in orographic precipitation might impact the spatial pattern of ξ and its response to global warming. Additional simulations with a wider range of climate models and parameterizations would be needed to evaluate the robustness of our results.

5 Conclusions

Results from a large ensemble of dynamically downscaled climate simulations reveals non-random spatial variability in the heaviness of the tail of the distribution of extreme daily precipitation. This variability has a very distinct windward vs. leeward pattern along the coastal mountains, the Sierra Nevada, and Cascades. This pattern is also present, but less strongly defined, in much of the Rocky Mountains. As characterized by the GEV shape parameter ξ, tails tend to be bounded ($\xi < 0$) on windward slopes and power-law ($\xi > 0$) elsewhere.

Anthropogenic forcing increases extreme precipitation (i.e., the 10 to 1000-year return interval intensity) across the western US, but the amount of increase varies from near zero to more than 40% at the grid cell scale, using the 20-year return period as an example. Nearer to the coast, the largest percentage increases tend to occur leeward of mountain ranges, but this pattern is not consistent throughout the interior west, where the direction of vapor transport is less consistent. At least a portion of the increase appears to be enhanced by a shift towards a heavier tail in most of the western US but dampened by a shift towards a less heavy tail in some areas (e.g., much of eastern Oregon and Washington, the Sierra Nevada, and Coast Mountains of BC).

The 25-km resolution climate model we used parameterizes convection, but general consistency of results in changes in extreme perception in California using a much higher resolution convective-permitting model (Huang et al. 2020) suggests much can still be learned by running coarser models, particularly where orography is important. With coarser models, the ability to generate very large ensembles becomes more feasible, so conducting both lower-resolution/large ensemble experiments and higher-resolution/small ensemble experiments can yield complementary insights (Lopez-Cantu et al. 2020). Computational requirements can be reduced as well by using, for example, pooling of neighboring grid cells (Li et al. 2019b) or pattern recognition (Wills et al. 2020) to extract forced responses from internal variability using smaller ensembles.

We report mainly on the spatial variability of extreme precipitation and its response to ~2 °C warming. While we note some potential mechanisms that might contribute to this response, further research is needed to better understand its causes. Methods to decompose responses into their thermodynamic and dynamic causes (Li et al. 2019a; Ben Alaya et al. 2020b), for example, may shed light on how mountains modulate the shape of the precipitation distribution and its response to global warming.

Supplementary Information The online version contains supplementary material available at https://doi.org/10.1007/s00382-022-06214-3.

Acknowledgements The authors thank David Wallom and Sarah Sparrow for providing support for weather@home. We would also like to thank the Met Office Hadley Centre PRECIS team for their technical and scientific support for the development and application of weather@home and thank all of the volunteers who have donated their computing time to climateprediction.net and weather@home.

Author contributions Conceptualization: DR. Methodology: DR, LH, and SL; Formal analysis and investigation: DR; Writing—original draft preparation: DR; Writing—review and editing: DR, LH, SL, MK, and NS.

Funding David Rupp was supported was supported by the National Oceanic and Atmospheric Administration's (NOAA) Regional Integrated Sciences and Assessments Program (RISA) under NOAA grants NA15OAR4310145 and NA15OAR4310145a.

Availability of data and material Gridded daily precipitation data from the PRISM Climate Group were accessed at http://prism.oregonstate.edu. Observed precipitation from the National Weather Service Cooperative Observer Program (COOP) are available at https://www.weather.gov/coop. Post-processed climate model simulations used in this study are archived at https://doi.org/10.5281/zenodo.5831031.

Code availability All analysis for this study was done with R (R Core Team 2021) and readily available R packages.

Declarations

Conflict of interest The authors have no relevant financial or non-financial interests to disclose.

Ethics approval Not applicable.

Consent to participate Not applicable.

Consent to publication Not applicable.

References

Ashfaq M, Rastogi D, Mei R et al (2016) High-resolution ensemble projections of near-term regional climate over the continental United States. J Geophys Res Atmos 121:9943–9963. https://doi.org/10.1002/2016JD025285

Ban N, Rajczak J, Schmidli J, Schär C (2020) Analysis of Alpine precipitation extremes using generalized extreme value theory in convection-resolving climate simulations. Clim Dyn 55:61–75. https://doi.org/10.1007/s00382-018-4339-4

Ben Alaya MA, Zwiers F, Zhang X (2020a) An evaluation of block-maximum-based estimation of very long return period

precipitation extremes with a large ensemble climate simulation. J Clim 33:6957–6970. https://doi.org/10.1175/JCLI-D-19-0011.1
Ben Alaya MA, Zwiers FW, Zhang X (2020b) A bivariate approach to estimating the probability of very extreme precipitation events. Weather Clim Extremes 30:100290. https://doi.org/10.1016/j.wace.2020.100290
Bracken C, Rajagopalan B, Alexander M, Gangopadhyay S (2015) Spatial variability of seasonal extreme precipitation in the western United States. J Geophys Res Atmos 120:4522–4533. https://doi.org/10.1002/2015JD023205
Brown SJ, Murphy JM, Sexton DMH, Harris GR (2014) Climate projections of future extreme events accounting for modelling uncertainties and historical simulation biases. Clim Dyn 43:2681–2705. https://doi.org/10.1007/s00382-014-2080-1
Cavanaugh NR, Gershunov A, Panorska AK, Kozubowski TJ (2015) The probability distribution of intense daily precipitation. Geophys Res Lett 42:1560–1567. https://doi.org/10.1002/2015GL063238
Chegwidden OS, Rupp DE, Nijssen B (2020) Climate change alters flood magnitudes and mechanisms in climatically-diverse headwaters across the northwestern United States. Environ Res Lett 15:094048. https://doi.org/10.1088/1748-9326/ab986f
Daly C, Halbleib M, Smith JI et al (2008) Physiographically sensitive mapping of climatological temperature and precipitation across the conterminous United States. Int J Climatol 28:2031–2064. https://doi.org/10.1002/joc.1688
Deser C, Phillips AS, Alexander MA, Smoliak BV (2014) Projecting North American climate over the next 50 years: uncertainty due to internal variability. J Clim 27:2271–2296. https://doi.org/10.1175/JCLI-D-13-00451.1
Diffenbaugh NS, Pal JS, Trapp RJ, Giorgi F (2005) Fine-scale processes regulate the response of extreme events to global climate change. PNAS 102:15774–15778. https://doi.org/10.1073/pnas.0506042102
Dominguez F, Rivera E, Lettenmaier DP, Castro CL (2012) Changes in winter precipitation extremes for the western United States under a warmer climate as simulated by regional climate models. Geophys Res Lett 39:L05803. https://doi.org/10.1029/2011GL050762
Dong B, Sutton RT, Shaffrey L, Wilcox LJ (2020) Attribution of 2012 extreme climate events: does air-sea interaction matter? Clim Dyn 55:1225–1245. https://doi.org/10.1007/s00382-020-05321-3
Donlon CJ, Martin M, Stark J et al (2012) The operational sea surface temperature and sea ice analysis (OSTIA) system. Remote Sens Environ 116:140–158. https://doi.org/10.1016/j.rse.2010.10.017
Dyrrdal AV, Skaugen T, Stordal F, Førland EJ (2016) Estimating extreme areal precipitation in Norway from a gridded dataset. Hydrol Sci J 61:483–494. https://doi.org/10.1080/02626667.2014.947289
Essery R, Clark DB (2003) Developments in the MOSES 2 land-surface model for PILPS 2e. Glob Planet Change 38:161–164. https://doi.org/10.1016/S0921-8181(03)00026-2
Fischer EM, Beyerle U, Schleussner CF et al (2018) Biased estimates of changes in climate extremes from prescribed SST simulations. Geophys Res Lett 45:8500–8509. https://doi.org/10.1029/2018GL079176
Fix MJ, Cooley D, Sain SR, Tebaldi C (2018) A comparison of U.S. precipitation extremes under RCP8.5 and RCP4.5 with an application of pattern scaling. Clim Change 146:335–347. https://doi.org/10.1007/s10584-016-1656-7
Gilleland E, Katz RW (2016) extRemes 2.0: an extreme value analysis package in R. J Stat Softw 72:1–39. https://doi.org/10.18637/jss.v072.i08
Gordon C, Cooper C, Senior CA et al (2000) The simulation of SST, sea ice extents and ocean heat transports in a version of the Hadley Centre coupled model without flux adjustments. Clim Dyn 16:147–168. https://doi.org/10.1007/s003820050010
Guillod BP, Jones RG, Bowery A et al (2017) weather@home 2: validation of an improved global–regional climate modelling system. Geosci Model Dev 10:1849–1872. https://doi.org/10.5194/gmd-10-1849-2017
Hawkins LR (2019) Modeling forest response to changing climate conditions in Western North America. PhD dissertation, Oregon State University
Hawkins LR, Rupp DE, McNeall DJ et al (2019) Parametric sensitivity of vegetation dynamics in the TRIFFID model and the associated uncertainty in projected climate change impacts on western U.S. Forests. J Adv Model Earth Syst 11:2787–2813. https://doi.org/10.1029/2018MS001577
He J, Soden BJ (2016a) The impact of SST biases on projections of anthropogenic climate change: a greater role for atmosphere-only models? Geophys Res Lett 43:7745–7750. https://doi.org/10.1002/2016GL069803
He J, Soden BJ (2016b) Does the lack of coupling in SST-forced atmosphere-only models limit their usefulness for climate change studies? J Clim 29:4317–4325. https://doi.org/10.1175/JCLI-D-14-00597.1
Hossain F, Degu AM, Yigzaw W et al (2012) Climate feedback–based provisions for dam design, operations, and water management in the 21st century. J Hydrol Eng 17:837–850. https://doi.org/10.1061/(ASCE)HE.1943-5584.0000541
Huang X, Ullrich PA (2017) The changing character of twenty-first-century precipitation over the western United States in the variable-resolution CESM. J Clim 30:7555–7575. https://doi.org/10.1175/JCLI-D-16-0673.1
Huang X, Swain DL, Hall AD (2020) Future precipitation increase from very high resolution ensemble downscaling of extreme atmospheric river storms in California. Sci Adv 6:eaba1323. https://doi.org/10.1126/sciadv.aba1323
Innocenti S, Mailhot A, Leduc M et al (2019) Projected changes in the probability distributions, seasonality, and spatiotemporal scaling of daily and subdaily extreme precipitation simulated by a 50-member ensemble over northeastern North America. J Geophys Res Atmos 124:10427–10449. https://doi.org/10.1029/2019JD031210
Jones R, Hassell D, Hudson D, et al (2003) Workbook on generating high resolution climate change scenarios using PRECIS. Hadley Centre for Climate Prediction and Research, Bracknell, UK, 39 pp
Koutsoyiannis D (2004) Statistics of extremes and estimation of extreme rainfall: II. Empirical investigation of long rainfall records. Hydrol Sci J 49:610. https://doi.org/10.1623/hysj.49.4.591.54424
Kunkel KE, Andsager K, Easterling DR (1999) Long-term trends in extreme precipitation events over the conterminous United States and Canada. J Clim 12:2515–2527. https://doi.org/10.1175/1520-0442(1999)012%3c2515:LTTIEP%3e2.0.CO;2
Laio F (2004) Cramer–von Mises and Anderson-Darling goodness of fit tests for extreme value distributions with unknown parameters. Water Resour Res 40:W09308. https://doi.org/10.1029/2004WR003204
Letcher TW, Minder JR (2015) Characterization of the simulated regional snow albedo feedback using a regional climate model over complex terrain. J Clim 28:7576–7595. https://doi.org/10.1175/JCLI-D-15-0166.1
Letcher TW, Minder JR (2017) The simulated response of diurnal mountain winds to regionally enhanced warming caused by the snow albedo feedback. J Atmos Sci 74:49–67. https://doi.org/10.1175/JAS-D-16-0158.1
Li H, Kanamitsu M, Hong S-Y et al (2014) Projected climate change scenario over California by a regional ocean–atmosphere coupled model system. Clim Change 122:609–619. https://doi.org/10.1007/s10584-013-1025-8

Li S, Mote PW, Rupp DE et al (2015) Evaluation of a regional climate modeling effort for the western United States using a superensemble from weather@home. J Clim 28:7470–7488. https://doi.org/10.1175/JCLI-D-14-00808.1

Li C, Zwiers F, Zhang X et al (2019a) Larger increases in more extreme local precipitation events as climate warms. Geophys Res Lett 46:6885–6891. https://doi.org/10.1029/2019GL082908

Li C, Zwiers F, Zhang X, Li G (2019b) How much information is required to well constrain local estimates of future precipitation extremes? Earth's Future 7:11–24. https://doi.org/10.1029/2018EF001001

Li S, Rupp DE, Hawkins L et al (2019c) Reducing climate model biases by exploring parameter space with large ensembles of climate model simulations and statistical emulation. Geosci Model Dev 12:3017–3043. https://doi.org/10.5194/gmd-12-3017-2019

Lopez-Cantu T, Samaras C (2018) Temporal and spatial evaluation of stormwater engineering standards reveals risks and priorities across the United States. Environ Res Lett 13:074006. https://doi.org/10.1088/1748-9326/aac696

Lopez-Cantu T, Prein AF, Samaras C (2020) Uncertainties in future U.S. extreme precipitation from downscaled climate projections. Geophys Res Lett 47:e2019GL086797. https://doi.org/10.1029/2019GL086797

Mahoney K, Scott JD, Alexander M et al (2021) Cool season precipitation projections for California and the western United States in NA-CORDEX models. Clim Dyn 56:3081–3102. https://doi.org/10.1007/s00382-021-05632-z

Massey N, Jones R, Otto FEL et al (2015) weather@home—development and validation of a very large ensemble modelling system for probabilistic event attribution. Q J R Meteorol Soc 141:1528–1545. https://doi.org/10.1002/qj.2455

Meinshausen M, Smith SJ, Calvin K et al (2011) The RCP greenhouse gas concentrations and their extensions from 1765 to 2300. Clim Change 109:213. https://doi.org/10.1007/s10584-011-0156-z

Mote PW, Allen MR, Jones RG et al (2016) Superensemble regional climate modeling for the western United States. Bull Am Meteor Soc 97:203–215. https://doi.org/10.1175/BAMS-D-14-00090.1

Papalexiou SM, Koutsoyiannis D (2013) Battle of extreme value distributions: a global survey on extreme daily rainfall. Water Resour Res 49:187–201. https://doi.org/10.1029/2012WR012557

Poschlod B, Ludwig R (2021) Internal variability and temperature scaling of future sub-daily rainfall return levels over Europe. Environ Res Lett. https://doi.org/10.1088/1748-9326/ac0849

Prein AF, Rasmussen RM, Ikeda K et al (2017) The future intensification of hourly precipitation extremes. Nat Clim Change 7:48–52. https://doi.org/10.1038/nclimate3168

R Core Team (2021) R: a language and environment for statistical computing. R Foundation for Statistical Computing, Vienna, Austria

Ragulina G, Reitan T (2017) Generalized extreme value shape parameter and its nature for extreme precipitation using long time series and the Bayesian approach. Hydrol Sci J 62:863–879. https://doi.org/10.1080/02626667.2016.1260134

Rupp DE, Li S, Mote PW et al (2017) Seasonal spatial patterns of projected anthropogenic warming in complex terrain: a modeling study of the western US. Clim Dyn 48:2191–2213. https://doi.org/10.1007/s00382-016-3200-x

Scinocca JF, Kharin VV, Jiao Y et al (2016) Coordinated global and regional climate modeling. J Clim 29:17–35. https://doi.org/10.1175/JCLI-D-15-0161.1

Shi X, Durran DR (2015) Estimating the response of extreme precipitation over midlatitude mountains to global warming. J Clim 28:4246–4262. https://doi.org/10.1175/JCLI-D-14-00750.1

Shi X, Durran D (2016) Sensitivities of extreme precipitation to global warming are lower over mountains than over oceans and plains. J Clim 29:4779–4791. https://doi.org/10.1175/JCLI-D-15-0576.1

Siler N, Roe G (2014) How will orographic precipitation respond to surface warming? An idealized thermodynamic perspective. Geophys Res Lett 41:2606–2613. https://doi.org/10.1002/2013GL059095

Singh D, Tsiang M, Rajaratnam B, Diffenbaugh NS (2013) Precipitation extremes over the continental United States in a transient, high-resolution, ensemble climate model experiment. J Geophys Res Atmos 118:7063–7086. https://doi.org/10.1002/jgrd.50543

Singh H, Najafi MR, Cannon AJ (2021) Characterizing non-stationary compound extreme events in a changing climate based on large-ensemble climate simulations. Clim Dyn 56:1389–1405. https://doi.org/10.1007/s00382-020-05538-2

Wallace B, Minder JR (2021) The impact of snow loss and soil moisture on convective precipitation over the Rocky Mountains under climate warming. Clim Dyn 56:2915–2939. https://doi.org/10.1007/s00382-020-05622-7

Wehner MF (2013) Very extreme seasonal precipitation in the NARCCAP ensemble: model performance and projections. Clim Dyn 40:59–80. https://doi.org/10.1007/s00382-012-1393-1

Wehner MF, Smith RL, Bala G, Duffy P (2010) The effect of horizontal resolution on simulation of very extreme US precipitation events in a global atmosphere model. Clim Dyn 34:241–247. https://doi.org/10.1007/s00382-009-0656-y

Wills RCJ, Battisti DS, Armour KC et al (2020) Pattern recognition methods to separate forced responses from internal variability in climate model ensembles and observations. J Clim 33:8693–8719. https://doi.org/10.1175/JCLI-D-19-0855.1

Wilson PS, Toumi R (2005) A fundamental probability distribution for heavy rainfall. Geophys Res Lett 32:L14812. https://doi.org/10.1029/2005GL022465

Wood RR, Ludwig R (2020) Analyzing internal variability and forced response of subdaily and daily extreme precipitation over Europe. Geophys Res Lett 47:e2020GL089300. https://doi.org/10.1029/2020GL089300

Wright DB, Bosma CD, Lopez-Cantu T (2019) U.S. hydrologic design standards insufficient due to large increases in frequency of rainfall extremes. Geophys Res Lett 46:8144–8153. https://doi.org/10.1029/2019GL083235

Wrzesien ML, Pavelsky TM (2020) Projected changes to extreme runoff and precipitation events from a downscaled simulation over the western United States. Front Earth Sci 7:355. https://doi.org/10.3389/feart.2019.00355

Wuertz D, Lawrimore J, Korzeniewski B (2018) Cooperative observer program (COOP) hourly precipitation data (HPD), version 2.0. NOAA National Centers for Environmental Information. https://doi.org/10.25921/p7j8-2170